Article

Impact of Cholesterol on the Stability of Monomeric and Dimeric Forms of the Translocator Protein TSPO: a Molecular Simulation Study

Zeineb Si Chaib[1,2,*], Alessandro Marchetto[3,*], Klevia Dishnica[3], Paolo Carloni[1,2,4], Alejandro Giorgetti[1,3,#], Giulia Rossetti[1,5,6#]

[1] Institute for Neuroscience and Medicine (INM-9) and Institute for Advanced Simulations (IAS-5) "Computational biomedicine", Forschungszentrum Jülich, 52425 Jülich, Germany.
[2] Faculty of Mathematics, Computer Science and Natural Sciences, RWTH Aachen, 52425 Aachen, Germany.
[3] Department of Biotechnology, University of Verona, 37134 Verona, Italy.
[4] Institute for Neuroscience and Medicine (INM-11)"Molecular Neuroscience and Neuroimaging", Forschungszentrum Jülich, 52425 Jülich.
[5] Jülich Supercomputing Center (JSC), Forschungszentrum Jülich, 52425 Jülich, Germany.
[6] Department of Hematology, Oncology, Hemostaseology, and Stem Cell Transplantation University Hospital Aachen, RWTH Aachen University, Pauwelsstraße 30, 52074 Aachen, Germany.

Correspondence: g.rossetti@fz-juelich.de (G.R), a.giorgetti@fz-juelich.de (A.G.)
* Equally contributed to this work

Abstract: The translocator protein (TSPO) is a transmembrane protein present in the three domains of life. Its functional quaternary structure consists of one or more subunits. In mouse, the dimer-to-monomer equilibrium is shifted *in vitro* towards the monomer by adding cholesterol, a natural component of mammalian membranes. Here, we present a coarse-grained molecular dynamics study on the mouse protein in the presence of a physiological content and of an excess of cholesterol. The latter turns out to weaken the interfaces of the dimer by clusterizing mostly at the inter-monomeric space and pushing the contact residues apart. It also increases the compactness and the rigidity of the monomer. These two factors might play a role for the experimentally observed incremented stability of the monomeric form with increased content of cholesterol. Comparison with simulations on bacterial proteins suggests that the effect of cholesterol is much less pronounced for the latter than for the mouse protein.

Keywords: TSPO; Martini Force-Field; cholesterol

1. Introduction

The translocator protein (TSPO), also known as peripheral benzodiazepine receptor, is a membrane protein conserved across the three domains of life [1]. During evolution, the TSPO gene family in bacteria and plants has expanded its roles [2] from an environmental sensor (such as sensitivity to salt stress in cyanobacteria and plants [3]) to a functional bioregulator, for instance facilitating the switch between photosynthesis and respiration, porphyrin transport and regulation of photosynthetic genes in the *Rhodobacter (Rs)* bacterium [4].

Mammalian TSPOs are mostly expressed in the outer mitochondrial membrane (OMM) [5]. Their functions may be rather diverse. For instance, in humans, the protein is involved in apoptosis, autophagy, inflammation along with cholesterol and porphyrin transport [6]. The latter is reminiscent of bacterial TSPO functions [7]. Human TSPO has emerged as an important neuropharmaceutical target. Indeed, TSPO levels are upregulated in activated glial cells, especially in microglia during neural disorders or injury [8]. As a result, radioligands binding to human TSPO in positron emission tomography (PET) scan may be used to diagnose CNS disorders [7].

Preprints (www.preprints.org) | NOT PEER-REVIEWED | Posted: 20 August 2020 doi:10.20944/preprints202008.0425.v1

TSPO consists of one or more units of about 18 KDa molecular weight. The topology of each unit, conserved across bacteria and mammals, consists of five transmembrane helices. These are tightly packed together (TM1-TM5) and connected by loops, located (for mammals) in the cytoplasm (LP-I and LP-III) and in the intermembrane space (LP-II and LP-IV) [7]. Structural information on TSPO is available from the bacteria *Bacillus Cereus* (*Bc*) and *Rhodobacter sphaeroides* (*Rs*), as well as from mice.

No monomer unit have been observed for *Rs*TSPO neither *in vitro* nor *in vivo* [9]. In the *Rs*TSPO X-ray structure, the protein is present as a dimer [9], suggesting that the minimum functional unit of the protein is a dimer [10]. The X-ray structure of the protein from *Bacillus Cereus* (*Bc*) has also been solved as a dimer [11], although crystal packing forces might have affected the oligomerization state [12]. In *mouse* TSPO, multimers (up to six units) exist *in vivo* [13,14] and these different oligomeric states may be associated with different functions [6,15]. The structure of the mouse monomer in the presence of detergent micelles has been solved by solution NMR [16].

Cholesterol represents the 10% of OMM [17]. OMM contains in addition phosphatidylcholine (PC, 40%), phosphatidylethanolamine (PE, 38.9%), phosphatidylserine (PS, 14.2%), phosphatidylinositol (PI, 5.9%) and cardiolipin (CDL) 0.8% [17]. Cholesterol has high (nanomolar) affinity for *mouse* TSPO [18] and it affects *mouse* TSPO oligomeric state. It stabilizes *in vitro* the monomer against the dimer [19], possibly by binding to a conserved "cholesterol-recognition motif" of the protein [18]. This is referred to as "LAF-CARC". CARC is defined by the linear array of residues (L/V)-X1−5-(Y)-X1−5-(K/R), located in the outer membrane leaflet and its reverse sequence, CRAC, (K/R)-X1−5-(Y/F)-X1−5-(L/V) in the inner one [20,21]. LAF (Leu-Ala-Phe) is a cholesterol binding enhancement motif associated with CRAC located one helix turn above the CRAC domain in mammalian TSPO [22]. Cholesterol is instead absent in bacterial membrane, and it binds to the proteins only in the micromolar range [10]. In *Rs*TSPO cell membrane, four major classes of phospholipids are present, namely, PE, PC, phosphatidylglycerol (PGL), and CDL, in a ratio of approximately 5:2:2.4:0.6 (PE/PC/PGL/CDL) [23]. In *Bc*TSPO, the major lipids that form the membrane are PE 43%, PGL 40% and CDL 17% [24].

Here, we investigate *mouse* and bacterial TSPOs embedded in membranes with different content of cholesterol by using coarse-grained simulations based on the Martini force field (version 2.2) [25]. The simulations are performed on *mouse* TSPO monomer and *mouse* TSPO dimers along with *Rs*TSPO and *Bc*TSPO dimers, embedded in a membrane resembling the composition of their respective realistic environment (OMM, Rs_mem and Bc_mem for *mouse* TSPO, *Rs*TSPO and *Bc*TSPO, respectively, see Table S1). Comparison is then made with models embedded in model membranes with physiological cholesterol content (10%, OMM), high cholesterol (28%, chl_mem) and without cholesterol (Bc_mem and Rs_mem) (Table S1).

The calculations on the bacterial proteins are based on the corresponding X-ray structures of the dimer [9,11]. Those on *mouse* TSPO are based on two models of the dimer built by us (available at [26]), based on *Rs*TSPO dimer X-ray and *mouse* TSPO monomer NMR structures. The first was fairly consistent with experimental data concerning the dimeric interface [19]; the second showed larger discrepancies with experiments. Both models were refined here in an OMM mimicking membrane by molecular simulation. Notably, the resulting structures were both able to reproduce the experimental dimer interface showing the impact of the membrane environment on structural models of membrane proteins. Models of the mouse proteins, embedded in Dodecylphosphocholine (DPC) [27] and 1,2-dimyristoyl-sn-glycero-3-phosphocholine (DMPC)/cholesterol mixtures [28], have been recently reported. Anticipating our results, our simulations suggest that cholesterol may stabilize the monomer by reducing the local and the global fluctuation of the protein; while it might destabilize the dimer by clusterizing at the subunit-subunit interface and pushing apart the contact residues. The impact of the molecule on the bacterial protein dimers appears to be much less evident.

2. Results

Preprints (www.preprints.org) | NOT PEER-REVIEWED | Posted: 20 August 2020 doi:10.20944/preprints202008.0425.v1

2.1. TSPO mouse dimers

Our previous work presented two models of the proteins with and without the nanomolar inhibitor PK-11195 [26]. These models were based on the *Rs*TSPO dimer X-ray structure (PDB accession code 4UC1) and on the NMR mouse TSPO monomer structure (PDB accession code 2MGY), in complex with PK-11195 [9,16]. The first, that we call here *m*TSPO(Rs), was obtained by homology modeling on *Rs*TSPO dimer; the second, *m*TSPO, was obtained by duplicating the monomeric *mouse* TSPO NMR structure and guiding the building of the dimer on the experimental chemical shifts in [19]. The proteins without ligands underwent refinement here in two different membrane environments (see Table S1). As shown in the next two sections, the resulting models are consistent with most of the available experimental data, which concern the dimer interface [19].

2.1.1. Models refinement.

In our previous structural prediction of **mTSPO(Rs)** [26], the G83XXXG87 and the W95XPXF99 dimerization motif were located at the dimer interface, consistently with the experimental data [19]. The monomer-monomer interface turned out to involve V80, G83, W93, I98, and A102 from TM-III and D111, V118 from TM-IV, consistently with NMR data [19] (Table 1). However, few residues - known to be part of the interface- were not sufficiently close to it, despite being localized near to it [26]. The protein exhibited an electrostatic profile favorable for membrane embedding (Figure 1B) [26].

Here, we refined the models by embedding the systems in both OMM and chl_mem and performing 8 μs MD with the Martini 2.2 coarse-grained force field [25] (see methods). The chosen model membranes feature physiological (10% of total phospholipids - OMM) and high (28% - chl_mem) cholesterol content (see Table S1 for composition). After ~1 μs, the structure was equilibrated as shown by the Root Mean Square Deviation (RMSD) (Figure S1). The RMSD between the initial and final structure was not very high (4 Å in the TM region), suggesting significant but not very large displacement from the initial position. The structure at the end of the dynamics displayed a compact dimer-dimer interface involving a higher number of residues than the starting structure. These include V80, G83, W93, W95, I98, F100, G101 from TM-III and D111, V118 from TM-IV, reported to be at the interface, accordingly to the NMR data [19] (Table 1).

The **mTSPO** starting model, built in [26], did not reproduce several of the experimental data: indeed, the residues experimentally identified at the monomer-monomer interface, were separated by a distance of 9 Å or more (N92, W93, W95, I98, F100, G101, and A102, Table 1) [26]; in addition, several charged residues were exposed in the transmembrane region, not allowing for a favorable embedding in the membrane [26]. Here, the refinement by MD leads large conformational rearrangements: the helices tend to twist to bury the exposed polar residues toward the core of the bundle (Figure 1A), while in parallel, the two monomers tend to get closer to maximize the contact between residues at the interface (Table 1). Helices one, three and five significantly bend in the intermembrane region of the receptor (Figure 2).

The structures were equilibrated after ~1 μs and ~2 μs in OMM and in chl_mem, respectively, as shown by the plot of RMSDs as a function of the simulated time (Figure S1). Notably, the MD structures at the end of the dynamics showed similar monomer-monomer interface's features as *m*TSPO(Rs) equilibrated structure (Table 1) and a favourable electrostatic profile for membrane embedding.

Table 1. Residues of *mouse* TSPO located at the dimer interface identified experimentally [19] (left), predicted by *m*TSPO (center) and *m*TSPO(Rs) structures at the end of the dynamics. Residues at the interface according to both experiment and simulations are in bold.

Region	Inferred by Experiment	*m*TSPO	*m*TSPO(Rs)

Preprints (www.preprints.org) | NOT PEER-REVIEWED | Posted: 20 August 2020 doi:10.20944/preprints202008.0425.v1

		Initial structures	
		F74, T75, E76, D77, M79, **V80**, P81, **G83**, L84, T86, G87, Q88, A90, L91	V6, P7, G10, L11, L13, V14, L17, G18, F20, M21, Y24 V26, R27(A) M79, **V80**, L82, **G83**, L84, Y85, T86, G87, A90, L91, **W93**, A94, P97, **I98**, **A102**, Q104, W107, A108, A110, **D111**, L114, **V118**, A121, A125
Dimer interface	V80, G83, Q88, N92, W93, W95, I98, F100, G101, A102, D111, V118	Structures after equilibration in OMM membrane	
		M1, P2, S4, W5, P7, A8, G10, L11, T12, L13, V14, P15, L17, G18, M21, G22, F25, V26, E29, Y34, L37, K39, P40, R46, V67, W68, E70, L71, D77, A78, M79, **V80**, P81, L82, **G83**, Y85, T86, G87, **Q88**, L89, A90, L91, **N92**, **W93**, A94, **W95**, P96, P97, **I98**, F99, **F100**, **G101**, **A102**, R103, Q104, M105, G106, W107, A108, L109, A110, **D111**, L113, L114, V115, S116, G117, **V118**, A121, T122, L124, A125, W126, R128, V129, S130, P131, N151, R166, L167, A168, E169	S4, V6, P7, V9, G10, L11, T12, L13, V14, P15, L17, G18, F20, M21, G22, Y24, F25, V26, R27, G28, E29, G30, L31, R32, W33, W47, W53, Y57, M60, S64, Y65, V67, W68, K69, E70, L71, G72, G73, F74, T75, E76, A78, M79, **V80**, P81, L82, **G83**, L84, Y85, T86, G87, L89, A90, L91, **W93**, A94, **W95**, P96, P97, **I98**, **F100**, **G101**, R103, Q104, M105, G106, W107, A110, **D111**, L114, **V118**, A121, W126,

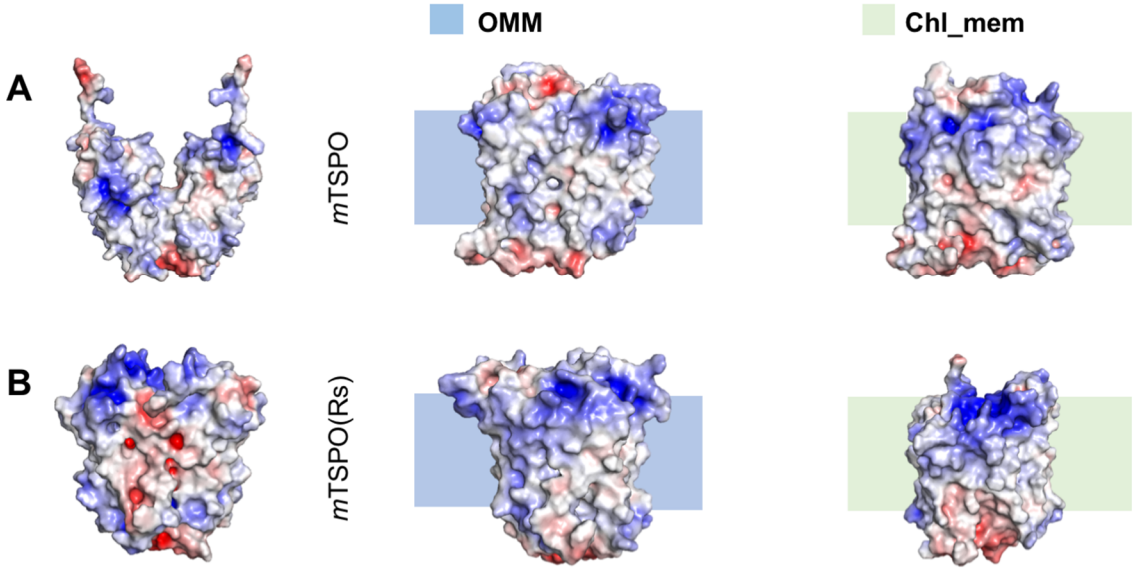

Preprints (www.preprints.org) | NOT PEER-REVIEWED | Posted: 20 August 2020 doi:10.20944/preprints202008.0425.v1

Figure 1. Electrostatic surface potential of the initial [26] and final MD structures of **(A)** *m*TSPO, **(B)** *m*TSPO(Rs) in the different membrane environments simulated here**.** The MD structures were backmapped to all-atom resolution using the backward.py script [29]. The red and blue surfaces represent negative and positive electrostatic potentials, respectively. The maximum values of the potentials are -5 kT/e, +5kT/e, respectively.

2.1.2. Structural properties of the models.

We present here the differences in structure and conformational fluctuations of *m*TSPO and *m*TSPO(Rs) dimers during the equilibrated trajectory, namely for the last 6 μs.

The RMSDs (Figure S1 and Table 2), the Root Mean Square Fluctuations (RMSFs) (Figure S2 A-B, and S3) and the gyration radii (Figure S2 C-D and Table 2) of the two models do not vary significantly by changing membrane environment (Figure S1-S2). High flexibility regions are observed for the loops and the termini, as expected (Figure S2).

A Principal Component Analysis (PCA) is used to identify differences in large scale motions of the proteins (Figure S3). We represent the first two eigenvectors (which cover between 31% and 38% of the motions of the proteins) as porcupine plots to show the direction and magnitude of selected eigenvectors for each of the backbone beads. *m*TSPO's conformational flexibility was larger than that of *m*TSPO(Rs) in OMM (Figure 2), as it can be seen by the porcupine plots of the first and second eigenvector (Figure S4). The flexibilities were similar for the two proteins embedded in chl_mem (Figure 2 and Figure S4), however at the dimer interface of both dimers, the two first eigenvectors "push" the residues far apart, hinting toward a destabilization of the dimers' interface (Figure 2 and Figure S4). Accordingly, the number of contacts at the dimer interface decreases in chl_mem (Figure 3).

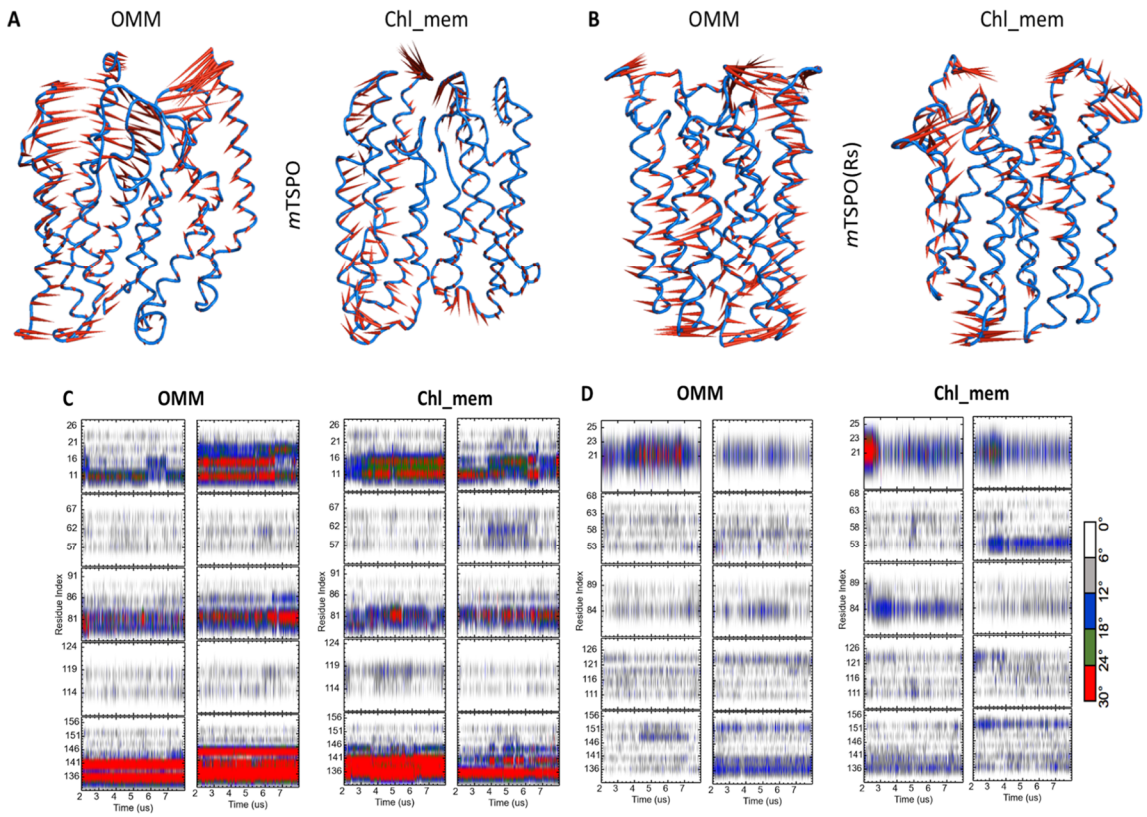

Figure 2. Porcupine plots depicting prominent motions averaged across the first normal mode for **(A)** *m*TSPO, **(B)** *m*TSPO(Rs) embedded in OMM and chl_mem; the correspondent plots for the second

 doi:10.20944/preprints202008.0425.v1

normal mode are reported in Figure S4. The helix bending of **(C)** *m*TSPO, **(D)** *m*TSPO(Rs) in OMM and chl_mem is plotted as a function of the simulation time.

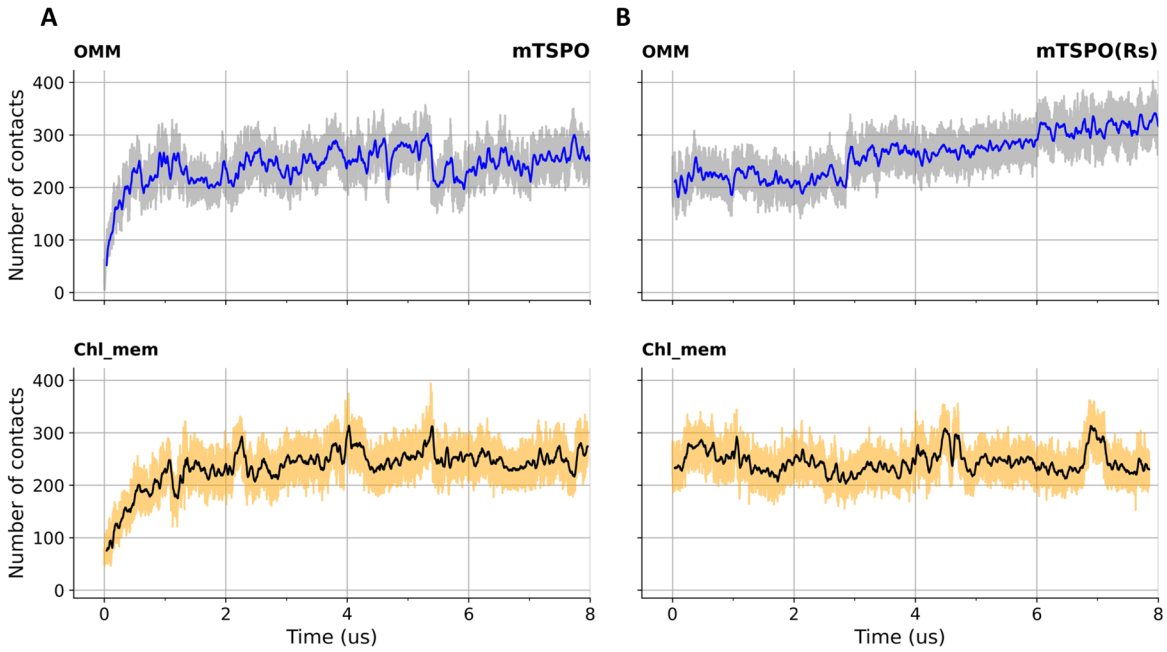

Figure 3. Number of monomer-monomer contact beads as a function of the simulation time in OMM and chl_mem for **(A)** *m*TSPO, **(B)** *m*TSPO(Rs). A cutoff of 0.6 nm was used.

2.2. mouse TSPO Monomers

2.2.1. Models refinement.

We predicted here the monomer structures based on the *Rs*TSPO structure [9] (*m*TSPO(Rs)_mon hereafter) and the NMR structure of monomeric mouse TSPO [16] (*m*TSPO_mon). The electrostatic surface of *m*TSPO(Rs)_mon starting model was favorable to membrane embedding, while this was not the case for *m*TSPO_mon [26], similarly to what observed for the initial structures of the corresponding dimers. The proteins were embedded in OMM and in chl_mem. They underwent 8 μs MD with the Martini coarse-grained force field version 2.2 [25], as in the case of the dimers.

***m*TSPO(Rs)_mon** turned out to be equilibrated after about 1 μs, as shown by the plot of the RMSD as a function of simulated time (Figure 4).

Preprints (www.preprints.org) | NOT PEER-REVIEWED | Posted: 20 August 2020 doi:10.20944/preprints202008.0425.v1

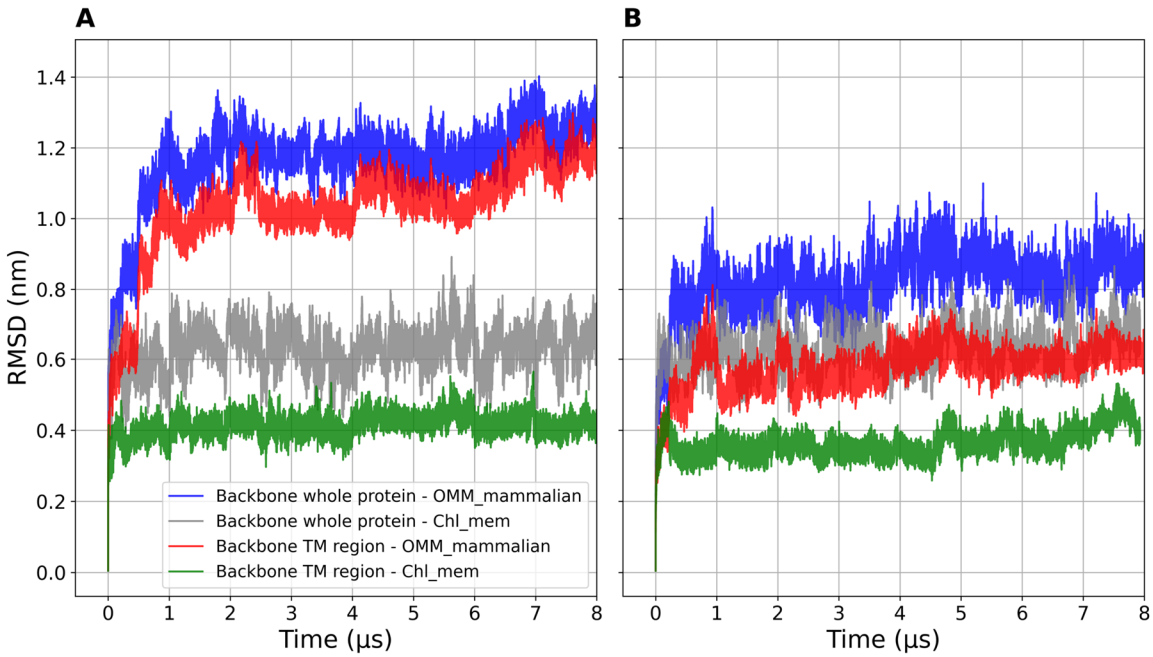

Figure 4. Backbone beads RMSD of **(A)** *m*TSPO_mon and **(B)** *m*TSPO(Rs)_mon (whole protein and TM regions) embedded in OMM and chl_mem plotted as a function of the simulated time. The RMSDs are computed with respect to the initial structures.

***m*TSPO_mon** required instead 2 μs to be equilibrated (Figure 4). It indeed underwent several conformational rearrangements similarly to what happened for the corresponding dimer. As a result, the protein becomes more compact. Also, the electrostatic surface of the TM region in the equilibrated structures became suitable for membrane embedding (Figure 5A), in contrast to the initial NMR structure [26].

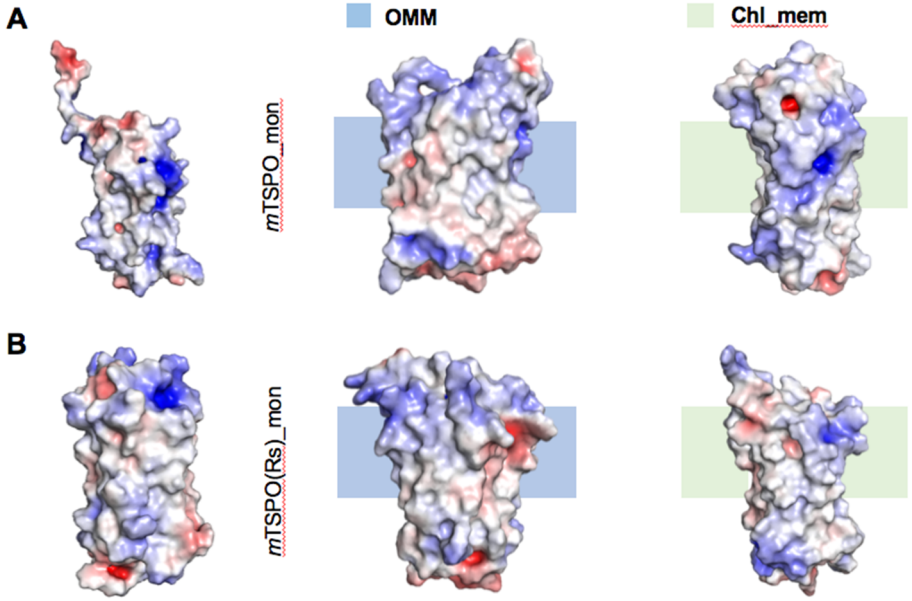

Figure 5. Electrostatic surface potential of the initial and equilibrated conformations, extracted from the trajectories after convergence (7.5 μs) and backmapped to all-atom resolution with the amber force field [30] using backward.py [29] of *m*TSPO_mon (A) and *m*TSPO(Rs)_mon (B) embedded in OMM and chl_mem. Red and blue surfaces represent negative and positive electrostatic potentials (-5 kT/e, +5kT/e) respectively.

Preprints (www.preprints.org) | NOT PEER-REVIEWED | Posted: 20 August 2020 doi:10.20944/preprints202008.0425.v1

197 2.2.2. Structural features

198 We present here the differences in structure and conformational fluctuations of *m*TSPO_mon
199 and *m*TSPO(Rs)_mon during the equilibrated trajectory, namely for the last 6 μs.

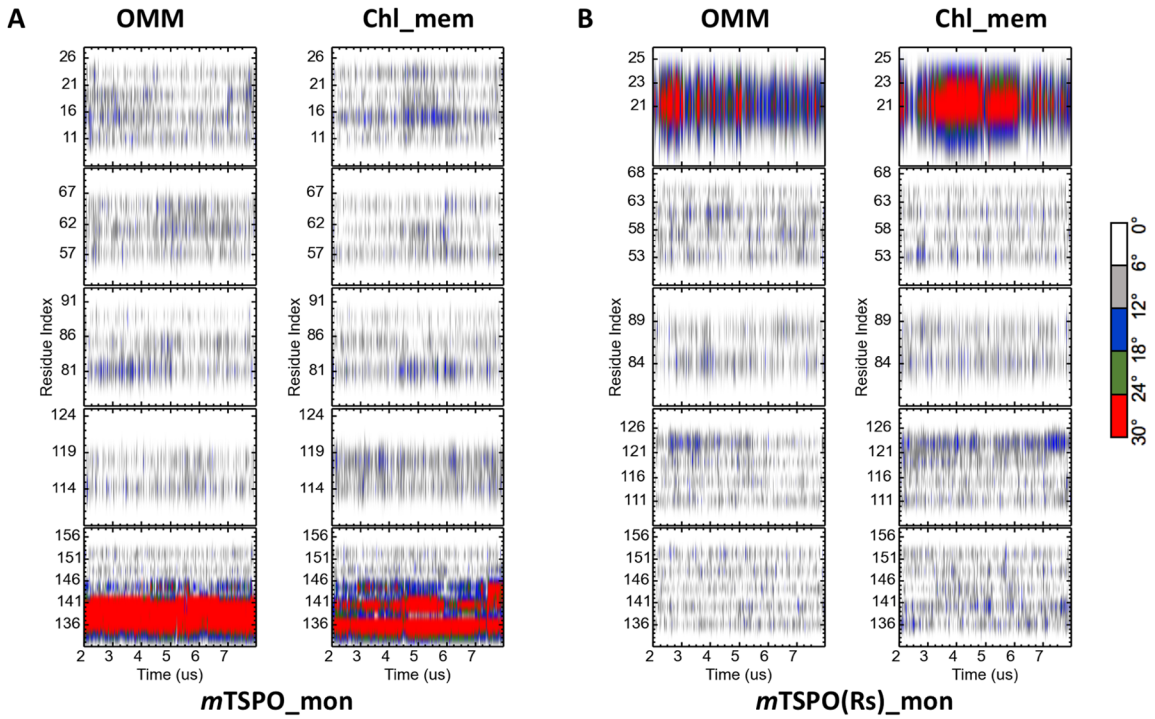

200

201 **Figure 6.** The helix bending of **(A)** *m*TSPO_mon and **(B)** *m*TSPO(Rs)_mon embedded in both OMM
202 and chl_mem as a function of the simulation time. Only the last 6 μs are shown.

203 The two models differ significantly: *m*TSPO_mon features a kink in helix five (Figure 6A), while
204 *m*TSPO(Rs)_mon in helix one (Figure 6B). The averaged backbone beads RMSDs decrease in all
205 circumstances with cholesterol content (Figure 4 and Table 2). Instead, the radii of gyration are rather
206 similar (Figure S5). The averaged RMSF values decrease in correspondence of the transmembrane
207 regions (TM1: 7-26, TM2: 46-63, TM3: 82-101, TM4: 106-124 and TM5: 134-153 for *m*TSPO and TM1:
208 8-23, TM2: 48-62, TM3: 83-98, TM4: 107-123 and TM5: 136-152 for mTSPO(Rs)) on passing from the
209 systems embedded in OMM to chl_mem (Figure S6). High flexibility regions are observed in the loops
210 and terminal regions, as expected (see Figure S6). The region 125-140 was more flexible in
211 *m*TSPO_mon than in *m*TSPO(Rs)_mon, which harbors the cholesterol-binding motif [19].

212 The first three vectors in the PCA collect between 35,8% and 50,4% of the conformational space
213 of the proteins (Figure S7). They are larger for the proteins embedded in OMM than those embedded
214 in the chl_mem (Figure 7 and Figure S8). Therefore, we suggest that the binding of cholesterol reduces
215 the conformational fluctuations of the proteins.

216 **Table 2.** RMSD and radii of gyration values of the systems investigated here, averaged over the
217 equilibrated trajectories (namely the last 6 μs for mouse monomeric and dimeric systems and
218 1.3 μs for the bacterial systems).

System	RMSD (nm)	Total Radius of gyration (nm)
*m*TSPO_mon, OMM	1.2 ± 0.05	1.7 ± 0.03
*m*TSPO_mon, chl_mem	0.6 ± 0.05	1.8 ± 0.03

Preprints (www.preprints.org) | NOT PEER-REVIEWED | Posted: 20 August 2020 doi:10.20944/preprints202008.0425.v1

*m*TSPO(Rs)_mon, OMM	0.8 ± 0.05	1.7 ± 0.02
*m*TSPO(Rs)_mon, chl_mem	0.6 ± 0.05	1.7 ± 0.02
*m*TSPO, chain A, OMM	1.1 ± 0.05	1.7 ± 0.02
*m*TSPO, chain B, OMM	1.0 ± 0.05	1.8 ± 0.02
*m*TSPO, chain A, chl_mem	1.2 ± 0.04	1.7 ± 0.01
*m*TSPO, chain B, chl_mem	1.1 ± 0.06	1.8 ± 0.02
*m*TSPO(Rs), chain A, OMM	0.8 ± 0.05	1.8 ± 0.02
mTSPO(Rs), chain B, OMM	0.6 ± 0.05	1.7 ± 0.01
*m*TSPO(Rs), chain A, chl_mem	0.6 ± 0.04	1.7 ± 0.02
*m*TSPO(Rs), chain B, chl_mem	0.5 ± 0.05	1.7 ± 0.01
*Bc*TSPO, chain A, Bc_mem	0.6 ± 0.01	1.6 ± 0.01
*Bc*TSPO, chain B, Bc_mem	0.6 ± 0.02	1.6 ± 0.01
*Bc*TSPO, chain A, chl_mem	0.5 ± 0.03	1.6 ± 0.01
*Bc*TSPO, chain B, chl_mem	0.6 ± 0.02	1.6 ± 0.01
*Rs*TSPO, chain A, Rs_mem	0.7 ± 0.04	1.7 ± 0.01
*Rs*TSPO, chain B, Rs_mem	0.5 ± 0.02	1.7 ± 0.01
*Rs*TSPO_chain A, chl_mem	0.6 ± 0.04	1.7 ± 0.01
*Rs*TSPO_chain B, chl_mem	0.6 ± 0.03	1.7 ± 0.02

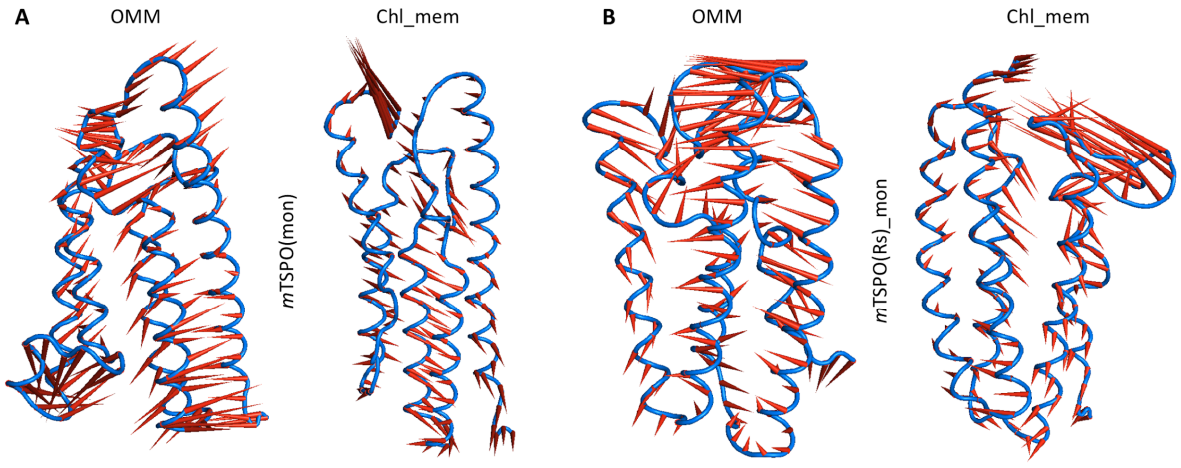

Preprints (www.preprints.org) | NOT PEER-REVIEWED | Posted: 20 August 2020 doi:10.20944/preprints202008.0425.v1

Figure 7. Porcupine plots depicting prominent motions averaged across the first normal mode for **(A)** *m*TSPO_mon and **(B)** *m*TSPO(Rs)_mon, in both OMM and chl_mem. The analysis was performed on the equilibrated part of the trajectory. The second normal mode is reported in Figure S8.

2.3. Cholesterol Occupancy

Given the significant effects of cholesterol described above, we finally analyzed the occupancy of cholesterol molecules in the two different membrane environments, for both monomer and dimer *mouse* TSPO models. In an overabundance of cholesterol (that is, for the proteins embedded in chl_mem), cholesterol molecules are spread rather homogeneously around the TM regions (Figure 8). This is fully consistent with the Coarse-Grained Dynamics simulation study by Rao et al. [28] on the same protein, performed in a DMPC/cholesterol mixture. These authors found that "cholesterol molecules are spread homogeneously in the membrane despite the presence of dimers" [28]. In contrast, for the proteins embedded in a membrane with physiological content of cholesterol (OMM), cholesterol clusters at TM1, TM3 and TM4 located at the dimer interface (Figure 8), and, for the *m*TSPO_mon, also at TM5. This helix contains the two well-known cholesterol-binding motifs, CRAC (residues 149–157) and its reverse counterpart CARC (residues 135–146) [20,21].

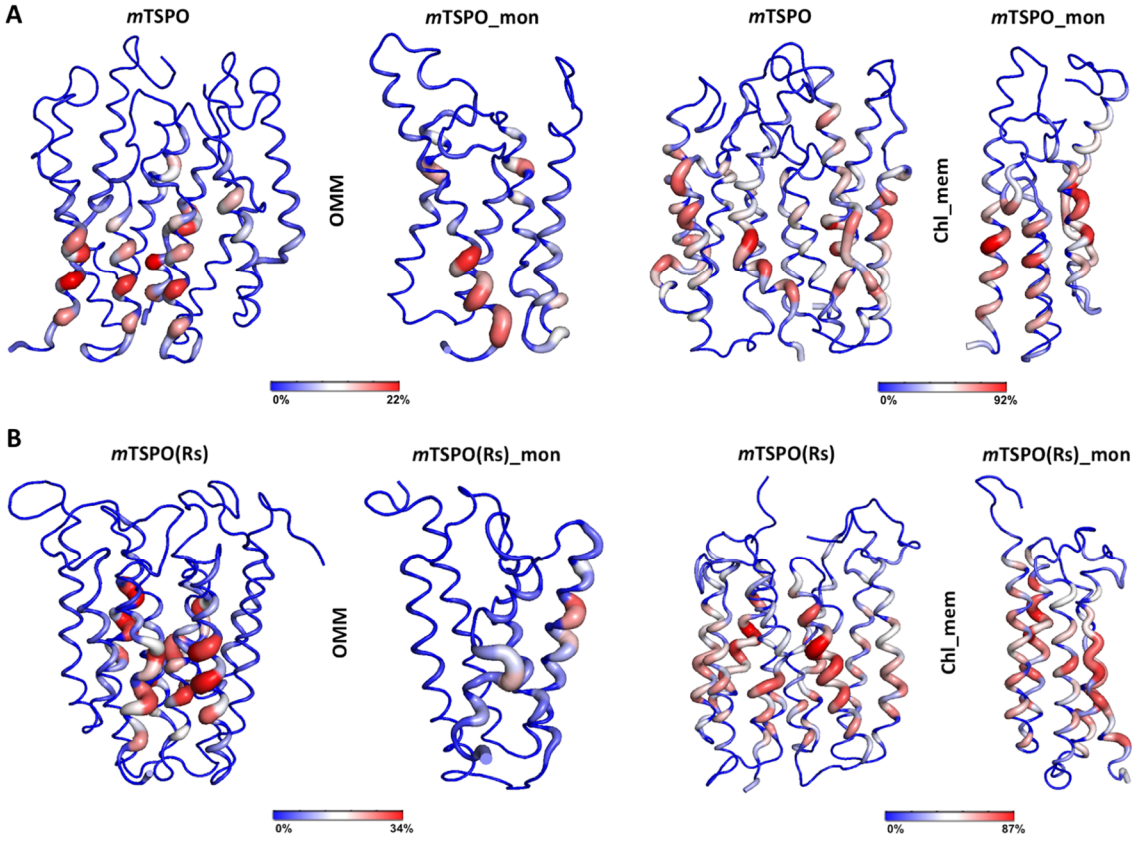

Figure 8. Cholesterol occupancy (i.e. percentage of frames where the lipid is in contact with a given residue (0-100%)) for **(A)** *m*TSPO, *m*TSPO_mon and **(B)** *m*TSPO(Rs), *m*TSPO(Rs)_mon in both OMM and chl_mem. The analysis was performed on the equilibrated part of the trajectory, that is, the last 6 μs.

2.4. Bacterial TSPO dimers

*Bc*TSPO and *Rs*TSPO embedded in the Bc_mem and Rs_mem (without cholesterol, as in natural bacterial membranes [24,31] respectively, and chl_mem (with 28% cholesterol) (Table S1) underwent 2 μs coarse-grained MD simulations. As shown by the RMSD plot as a function of simulated time (Figure S9), the systems reached equilibrium already after 700 ns, possibly

Preprints (www.preprints.org) | NOT PEER-REVIEWED | Posted: 20 August 2020 doi:10.20944/preprints202008.0425.v1

because in this case we started from X-ray structures and not theoretical models. The average displacement from the initial structures were ~0.6 nm for both structures (Figure S9).

The RMSD, RMSF and gyration radius (Figure S9-S11) as well as the calculated electrostatic surfaces along the simulation (Figure S12) are similar across the four systems investigated here. Also the bending of the helices does not change on passing from the bacterial membranes to chl_mem (Figure S15). The contacts at the interface of the proteins embedded in Bc_mem and Rs_mem are larger than those in chl_mem (Figure S13). In our PCA analysis (Figure S14), the first two eigenvectors exhibit very small fluctuations at the interface in both membranes (Figure 9). Based on all of these observations, we conclude that the presence of cholesterol impacts on the structural determinants and conformational fluctuations of the proteins to a lesser extent than in the *mouse* proteins.

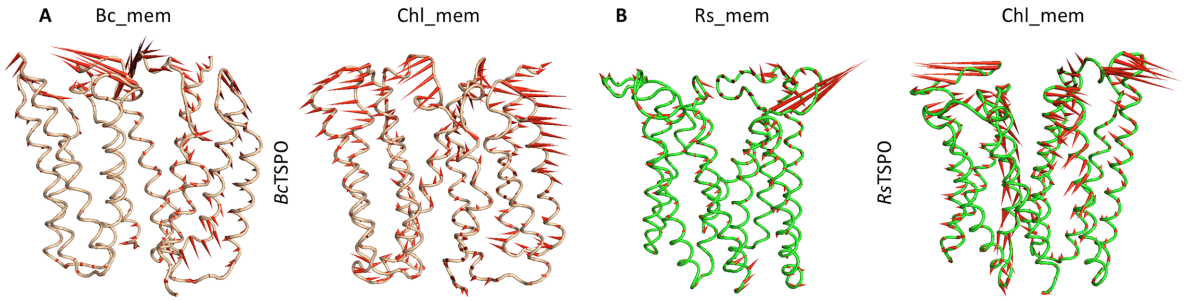

Figure 9. Porcupine plots depicting prominent motions averaged across the first normal mode for: (**A**) *Bc*TSPO in Bc_mem and chl_mem and (**B**) *Rs*TSPO in Rs_mem and chl_mem, respectively. The analysis was performed on the equilibrated part of the trajectory, namely the last 1.3 μs.

3. Discussion

Cholesterol is an essential component of mammalian membranes [32]. Among the TSPO functions gained during speciation and evolution leading to mammals, is the binding and trafficking of this molecule [1]. Recent work by Jaipura *et al* has shown that cholesterol stabilizes the monomeric state against the dimer in *mouse* TSPO [19]. Here, we present a coarse-grained MD study on these proteins embedded in membranes at different cholesterol content to get insight on this intriguing effect of this molecule. Comparison is made with bacterial proteins, suggested to exist in dimeric form and binding with much less affinity cholesterol than *mouse* TSPO.

Dimer and monomer models, built by us in [26] and refined here by coarse-grained MD, were embedded in two types of membranes: (i) OMM, which contains six different types of lipids and around 10% of cholesterol. This provides a quasi *in*-vivo mimetic membrane environment; (ii) chl_mem, with a high cholesterol content (28% instead of 10%).

The dimeric models were fully consistent with the experimental data, which are available only for this state [19] (Table 1). Besides, our model based on the *mouse* NMR monomer structure [16], exhibits a similar interface to that of a recent dimeric model presented [28] involving TM1 and TM3 helices. Both dimer and monomer initial models displayed an electrostatic potential which is well suitable for embedding in the cell membrane. This contrasts with the NMR structure of the monomer [16] (used here as a starting model for some of our simulations) , this supports the hypothesis that the ionic detergents used in the structure determination have altered some key structural features relevant for the stability of the protein in a membrane environment [12,27].

Preprints (www.preprints.org) | NOT PEER-REVIEWED | Posted: 20 August 2020 doi:10.20944/preprints202008.0425.v1

Both the simulations of the monomers and the dimers hint (albeit they do not demonstrate) a stabilization of the latter by adding cholesterol. First, at the physiological content of cholesterol, this is located mostly at residues at the dimeric interface, while in *m*TSPO_mon, cholesterol is found at the two cholesterol-binding motifs, CRAC and CARC [20,21]; second, an overabundance of cholesterol causes a decrease of subunit-subunit contacts in the dimer: Consistently, the large-scale motions might favor a detachment of the two units by pushing apart the residues in contact at the interface, as shown by our PCA analyses. All these features point to a destabilizing effect of cholesterol on the dimeric structure. Finally, under the reasonable (but not demonstrated) assumption that the compactness and rigidity of proteins may correlate with its thermodynamic stability [33], one can suggest that cholesterol stabilizes the monomer. Indeed, (i) the size of the monomeric *mouse* TSPO models, in terms of RMSD and gyration radii, decreases with cholesterol content, in contrast to what happens in the dimeric forms; (ii) the fluctuations, as measured by RSMF values, are lower; (iii) the large-scale motions exhibit a smaller amplitude in the presence of cholesterol for both the monomeric proteins.

The presence of cholesterol appears to affect the size and rigidity of the corresponding bacterial proteins to a lower extent. These are naturally embedded in a cholesterol-free membrane and present most probably as dimers [9]. Indeed, RMSD gyration radii do not vary significantly upon the addition of cholesterol. In addition, RMSF and large-scale motion are not significantly affected by the presence of this molecule. However, the contacts at the subunit-subunit decrease with an excess of cholesterol (albeit to a smaller extent than what observed in the mouse protein). Hence, the study for the bacterial proteins is not conclusive.

4. Materials and Methods

System Setup of Coarse-Grained Models. The structure of mouse TSPO (*m*TSPO_mon) was the NMR structure (PDB accession code: 2MGY). The first conformation was chosen as it corresponds to the best representative conformer in the ensemble and the ligand PK-11195 was removed. The dimer *m*TSPO was constructed based on the NMR study reported in [16] . Another model of mouse TSPO was built by us (*m*TSPO(Rs)_mon and *m*TSPO(Rs) for monomeric and dimeric forms respectively), by homology modeling, based on the X-ray coordinates of the prokaryotic *Rs*TSPO (PDB accession code: 4UC1) [9].

The structures of bacterial TSPO were taken from the X-ray structures 4RYI (*Bc*TSPO) [11] and 4UC3 (*Rs*TSPO) [9]. Missing residues of 4UC3 between GLU29 and ASN40 in chains A and B were modelled using as template the structure 4UC2 [9] while those between MET147 and ARG157 of chain B were modelled using the same region in chain A of 4UC3 [9]. The Modeller program version 9.19 [34] was used to build the missing regions and the best model according to the Discrete optimized protein energy (DOPE) [35] and GA341 [36] score was selected. The default protonation states at pH 7 were used for the ionizable residues. Protein structures were converted to coarse-grained Martini representations using the martinize.py script [25] . The coarse-grained protein coordinates were then positioned in the center of a simulation box of size 14 x 14 x 16 nm^3 with its principal transmembrane axis aligned parallel to the z-axis and embedded in different symmetric lipid bilayers: (i) chl_mem contains: phosphatidylcholine (POPC, 31%), phosphatidylethanolamine (POPE, 41%) and cholesterol (CHOL, 28%). (ii) A realistic mammalian outer mitochondrial membrane (OMM) composed of six different lipid species [17,37-40]: POPC, 40%, 1-stearoyl-2-docosahexaenoyl-phosphatidylethanolamine (SDPE, 38.9%), 1-stearoyl-2-docosahexaenoyl-phosphatidylserine (SDPS, 14.2%), stearoyl-arachidonoyl phosphatidylinositol (SAPI, 5.9%), doubly deprotonated cardiolipin (CDL2, 0.8%) and CHOL, 10% of total phospholipids, providing an *in vivo*-mimetic membrane environment. (iii) Rs_mem composed of POPC, 20%, POPE, 50%, palmitoyl oleoyl phosphatidylglycerol (POPG, 24%) and cardiolipin (CDL2, 6%) [31] and (iiii) Bc_mem containing POPE, 43%, POPG, 40% and CDL2, 17% [24]. 0.15 M NaCl was added to reach the physiological ions concentration and extra ions were added to neutralize the systems.

Preprints (www.preprints.org) | NOT PEER-REVIEWED | Posted: 20 August 2020 doi:10.20944/preprints202008.0425.v1

Coarse-Grained Simulation Parameters. The Martini coarse-grained force field version 2.2 [25] was used for protein and version 2.0 for lipids. All the simulations were performed using Gromacs 2019.3 [41]. The non-biased simulations were run in the isothermal-isobaric NPT ensemble equilibrium simulations. The temperature was controlled at 315K using V-rescale thermostat [42] with a coupling constant of τ_t = 1.0 ps. The pressure was semi-isotropically controlled (i.e. independently in the xy plane and z axis direction) by a Parrinello-Rahman barostat [43] at a reference of p = 1 bar with a coupling constant of τ_P = 12.0 ps and compressibility of 3 x 10^{-4}. Non-bonded interactions were used in their shifted form with electrostatic interactions shifted to zero in the range of 0-1.1 nm and Lennard-Jones interaction shifted to zero in the range of 0.9-1.1 nm. A time step of 20 fs was used with neighbor lists updated every 20 steps. Periodic boundary condition was used in the x, y and z axis. ~8 μs and 2 μs data were collected for mouse TSPO and bacterial TSPO simulations respectively. An overview of the simulations is listed in Table S1.

Analysis of molecular dynamics results. The root mean square deviation of backbone beads (RMSD), the root mean square fluctuations (RMSF) and the radius of gyration (RGYR) were calculated using gmx rms, rmsf and gyrate modules from the Gromacs package [41], respectively. Principal component analysis (PCA) was restricted to backbone beads, as it is less perturbed by statistical noise and provides significant characterization of the essential space motions [44]. It was performed using Gromacs tools gmx covar and gmx anaeig [41]. To visualize the direction and extent of the principal motions of the simulated systems, porcupine plot analysis was performed using modevectors script in Pymol [45]. When applied, for each simulated system, the initial structure was used as a reference. The helix bundle geometrical features were characterized by implementing the Bendix plug-in [46] in VMD software [47], that calculates and visualizes the helix axis evolution over time. It was performed using default parameters for coarse grained systems. Electrostatic calculations were performed on the initial structures and the ones after equilibrium. Conformations were first extracted and back-mapped to all-atom resolution in amber force field [30] using backward.py [29]. Electrostatics were then performed with the APBS Electrostatics plugin in Pymol [48] using default parameters.

The gmx mindist module in Gromacs [41] was used to compute the number of contacts in time between each monomer in the simulated dimers, using the default distance cutoff of 0.6 nm. The cholesterol occupancy (i.e. percentage of frames where lipid is in contact with the given residue (0-100%)) was calculated using the toolkit PyLipID [49] and a distance cutoff of 0.55 and 1.0 nm.

Conclusions

We have presented a molecular dynamics study on *mouse* TSPO monomeric and dimeric structures. Our models are fully consistent with the available experimental data [19]. In addition, they provide hints on why cholesterol shifts the monomer-dimer equilibrium toward the monomer in *mouse* TSPO. Simulations with the correspondent proteins from *Bc* and *Rs* bacteria might suggest that the destabilization of the dimer by cholesterol (a molecule not present in bacterial membranes) is not as pronounced as in the case of the mouse proteins.

Supplementary Materials: Table S1: Overview of the simulated systems, Figure S1: *m*TSPO and *m*TSPO(Rs) backbone RMSD, Figure S2: RMSF and radii of gyration plots of *m*TSPO and *m*TSPO(Rs), Figure S3: Projection of the first three eigenvectors of *m*TSPO and *m*TSPO(Rs), Figure S4: Porcupine plots depicting prominent motions averaged across the second normal mode for *m*TSPO and *m*TSPO(Rs), Figure S5: Radii of gyration of *m*TSPO_mon and *m*TSPO(Rs)_mon, Figure S6: RMSF plots of *m*TSPO_mon and *m*TSPO(Rs)_mon, Figure S7: Projection of the backbone beads trajectory along the first three eigenvectors for *m*TSPO_mon and *m*TSPO(Rs)_mon, Figure S8: Porcupine plots depicting prominent motions averaged across the second normal mode for *m*TSPO_mon and *m*TSPO(Rs)_mon, Figure S9: Backbone beads RMSD of the whole protein and TM regions for *Bc*TSPO and *Rs*TSPO, Figure S10: RMSF and radii of gyration plots for *Bc*TSPO and *Rs*TSPO, Figure S11: Projection of the first three eigenvectors for *Bc*TSPO and *Rs*TSPO. Figure S12: Electrostatic surface potentials in the initial and final MD structures for *Rs*TSPO and *Bc*TSPO, Figure S13: Number of subunit-subunit contacts

 doi:10.20944/preprints202008.0425.v1

plotted as a function of the simulation time for *Bc*TSPO and *Rs*TSPO, Figure S14: Porcupine plots depicting large scale motions averaged across the second normal mode for *Bc*TSPO and *Rs*TSPO, Figure S15: Helix bending of *Bc*TSPO and for *Rs*TSPO.

Author Contributions: Conceptualization, P.C., G.R. and A.G.; methodology, Z.S.C. and A.M.; software, Z.S.C. and A.M.; validation, Z.S.C.; formal analysis, Z.S.C., K.D. and A.M.; investigation, Z.S.C., K.D., A.M. and G.R.; resources, P.C., G.R. and A.G.; data curation, Z.S.C.; writing—original draft preparation, P.C., G.R., Z.S.C. and A.G.; writing—review and editing, all the authors.; visualization, Z.S.C.; supervision, P.C., G.R. and A.G.; project administration, P.C., G.R. and A.G.; funding acquisition, P.C., G.R. and A.G. All authors have read and agreed to the published version of the manuscript.", please turn to the CRediT taxonomy for the term explanation. Authorship must be limited to those who have contributed substantially to the work reported

Funding: This project/research has received funding from the European Union's Horizon 2020 Framework Programme for Research and Innovation under the Specific Grant Agreement No. 945539 (Human Brain Project SGA3).

Acknowledgments: We deeply acknowledge the contribution of 'Centro Piattaforme Tecnologiche dell' Università degli Studi di Verona'.

Conflicts of Interest: The authors declare no conflict of interest.

Abbreviations:

*m*TSPO	Dimeric mouse TSPO model based on NMR structure (PDBiD: 2MGY)
*m*TSPO_mon	Monomeric mouse TSPO model based on NMR structure (PDBiD: 2MGY)
*m*TSPO(Rs)	Dimeric mouse TSPO model based on *Rs*TSPO dimer (PDBiD: 4UC1)
*m*TSPO(Rs)_mon	Monomeric mouse TSPO model based on *Rs*TSPO dimer (PDBiD: 4UC1)
*Rs*TSPO	*Rhodobacter sphaeroides* dimer (PDBiD: 4UC3)
*Bc*TSPO	*Bacillus cereus* dimer (PDBiD: 4RYI)
OMM	Mammalian Outer Mitochondrial Membrane
Chl_mem	Cholesterol rich membrane
Rs_mem	*Rs* bacterial membrane
Bc_mem	*Bc* bacterial membrane

References

1. Fan, J.; Lindemann, P.; GJ Feuilloley, M.; Papadopoulos, V. Structural and functional evolution of the translocator protein (18 kDa). *Current molecular medicine* **2012**, *12*, 369-386.
2. Veenman, L.; Vainshtein, A.; Yasin, N.; Azrad, M.; Gavish, M. Tetrapyrroles as endogenous TSPO ligands in eukaryotes and prokaryotes: Comparisons with synthetic ligands. *International journal of molecular sciences* **2016**, *17*, 880.
3. Balsemão-Pires, E.; Jaillais, Y.; Olson, B.J.; Andrade, L.R.; Umen, J.G.; Chory, J.; Sachetto-Martins, G. The Arabidopsis translocator protein (AtTSPO) is regulated at multiple levels in response to salt stress and perturbations in tetrapyrrole metabolism. *BMC plant biology* **2011**, *11*, 108.
4. Yeliseev, A.A.; Krueger, K.E.; Kaplan, S. A mammalian mitochondrial drug receptor functions as a bacterial "oxygen" sensor. *Proceedings of the National Academy of Sciences* **1997**, *94*, 5101-5106.
5. Rupprecht, R.; Papadopoulos, V.; Rammes, G.; Baghai, T.C.; Fan, J.; Akula, N.; Groyer, G.; Adams, D.; Schumacher, M. Translocator protein (18 kDa)(TSPO) as a therapeutic target for neurological and psychiatric disorders. *Nature reviews Drug discovery* **2010**, *9*, 971.
6. Li, F.; Liu, J.; Garavito, R.M.; Ferguson-Miller, S. Evolving understanding of translocator protein 18 kDa (TSPO). *Pharmacological research* **2015**, *99*, 404-409.
7. Lee, Y.; Park, Y.; Nam, H.; Lee, J.-W.; Yu, S.-W. Translocator protein (TSPO): the new story of the old protein in neuroinflammation. *BMB reports* **2020**, *53*, 20.
8. Kim, E.-J.; Yu, S.-W. Translocator protein 18 kDa (TSPO): old dogma, new mice, new structure, and new questions for neuroprotection. *Neural Regeneration Research* **2015**, *10*, 878.
9. Li, F.; Liu, J.; Zheng, Y.; Garavito, R.M.; Ferguson-Miller, S. Crystal structures of translocator protein (TSPO) and mutant mimic of a human polymorphism. *Science* **2015**, *347*, 555-558.
10. Li, F.; Xia, Y.; Meiler, J.; Ferguson-Miller, S. Characterization and modeling of the oligomeric state and ligand binding behavior of purified translocator protein 18 kDa from Rhodobacter sphaeroides. *Biochemistry* **2013**, *52*, 5884-5899.
11. Guo, Y.; Kalathur, R.C.; Liu, Q.; Kloss, B.; Bruni, R.; Ginter, C.; Kloppmann, E.; Rost, B.; Hendrickson, W.A. Structure and activity of tryptophan-rich TSPO proteins. *Science* **2015**, *347*, 551-555.
12. Li, F.; Liu, J.; Liu, N.; Kuhn, L.A.; Garavito, R.M.; Ferguson-Miller, S. Translocator protein 18 kDa (TSPO): an old protein with new functions? *Biochemistry* **2016**, *55*, 2821-2831.
13. Delavoie, F.; Li, H.; Hardwick, M.; Robert, J.-C.; Giatzakis, C.; Péranzi, G.; Yao, Z.-X.; Maccario, J.; Lacapere, J.-J.; Papadopoulos, V. In vivo and in vitro peripheral-type benzodiazepine receptor polymerization: functional significance in drug ligand and cholesterol binding. *Biochemistry* **2003**, *42*, 4506-4519.
14. Boujrad, N.; Vidic, B.; Papadopoulos, V. Acute action of choriogonadotropin on Leydig tumor cells: changes in the topography of the mitochondrial peripheral-type benzodiazepine receptor. *Endocrinology* **1996**, *137*, 5727-5730, doi:10.1210/endo.137.12.8940407.
15. Rone, M.B.; Midzak, A.S.; Issop, L.; Rammouz, G.; Jagannathan, S.; Fan, J.; Ye, X.; Blonder, J.; Veenstra, T.; Papadopoulos, V. Identification of a dynamic mitochondrial protein complex driving cholesterol import, trafficking, and metabolism to steroid hormones. *Molecular Endocrinology* **2012**, *26*, 1868-1882.
16. Jaremko, Ł.; Jaremko, M.; Giller, K.; Becker, S.; Zweckstetter, M. Structure of the mitochondrial translocator protein in complex with a diagnostic ligand. *Science* **2014**, *343*, 1363-1366.
17. Corazzi, L.; Roberti, R. Lipids of Brain Mitochondria. In *Handbook of Neurochemistry and Molecular Neurobiology*, 2010.

18. Li, H.; Papadopoulos, V. Peripheral-type benzodiazepine receptor function in cholesterol transport. Identification of a putative cholesterol recognition/interaction amino acid sequence and consensus pattern. *Endocrinology* **1998**, *139*, 4991-4997.
19. Jaipuria, G.; Leonov, A.; Giller, K.; Vasa, S.K.; Jaremko, Ł.; Jaremko, M.; Linser, R.; Becker, S.; Zweckstetter, M. Cholesterol-mediated allosteric regulation of the mitochondrial translocator protein structure. *Nature communications* **2017**, *8*, 1-8.
20. Fantini, J.; Di Scala, C.; Evans, L.S.; Williamson, P.T.; Barrantes, F.J. A mirror code for protein-cholesterol interactions in the two leaflets of biological membranes. *Scientific reports* **2016**, *6*, 21907.
21. Jamin, N.; Neumann, J.-M.; Ostuni, M.A.; Vu, T.K.N.; Yao, Z.-X.; Murail, S.; Robert, J.-C.; Giatzakis, C.; Papadopoulos, V.; Lacapere, J.-J. Characterization of the cholesterol recognition amino acid consensus sequence of the peripheral-type benzodiazepine receptor. *Molecular endocrinology* **2005**, *19*, 588-594.
22. Li, F.; Liu, J.; Valls, L.; Hiser, C.; Ferguson-Miller, S. Identification of a key cholesterol binding enhancement motif in translocator protein 18 kDa. *Biochemistry* **2015**, *54*, 1441-1443.
23. Zhang, X.; Tamot, B.; Hiser, C.; Reid, G.E.; Benning, C.; Ferguson-Miller, S. Cardiolipin deficiency in Rhodobacter sphaeroides alters the lipid profile of membranes and of crystallized cytochrome oxidase, but structure and function are maintained. *Biochemistry* **2011**, *50*, 3879-3890.
24. Epand, R.F.; Pollard, J.E.; Wright, J.O.; Savage, P.B.; Epand, R.M. Depolarization, bacterial membrane composition, and the antimicrobial action of ceragenins. *Antimicrobial agents and chemotherapy* **2010**, *54*, 3708-3713.
25. de Jong, D.H.; Singh, G.; Bennett, W.D.; Arnarez, C.; Wassenaar, T.A.; Schäfer, L.V.; Periole, X.; Tieleman, D.P.; Marrink, S.J. Improved parameters for the martini coarse-grained protein force field. *Journal of chemical theory and computation* **2013**, *9*, 687-697.
26. Zeng, J.; Guareschi, R.; Damre, M.; Cao, R.; Kless, A.; Neumaier, B.; Bauer, A.; Giorgetti, A.; Carloni, P.; Rossetti, G. Structural prediction of the dimeric form of the mammalian translocator membrane protein TSPO: a key target for brain diagnostics. *International journal of molecular sciences* **2018**, *19*, 2588.
27. Xia, Y.; Ledwitch, K.; Kuenze, G.; Duran, A.; Li, J.; Sanders, C.R.; Manning, C.; Meiler, J. A unified structural model of the mammalian translocator protein (TSPO). *Journal of biomolecular NMR* **2019**, *73*, 347-364.
28. Rao, R.M.; Diharce, J.; Dugué, B.; Ostuni, M.A.; Cadet, F.; Etchebest, C. A VERSATILE DIMERISATION PROCESS OF TRANSLOCATOR PROTEIN (TSPO) REVEALED BY AN EXTENSIVE SAMPLING BASED ON A COARSE-GRAINED DYNAMICS STUDY. *Journal of Chemical Information and Modeling* **2020**.
29. Wassenaar, T.A.; Pluhackova, K.; Böckmann, R.A.; Marrink, S.J.; Tieleman, D.P. Going backward: a flexible geometric approach to reverse transformation from coarse grained to atomistic models. *Journal of chemical theory and computation* **2014**, *10*, 676-690.
30. Wang, J.; Wolf, R.M.; Caldwell, J.W.; Kollman, P.A.; Case, D.A. Development and testing of a general amber force field. *Journal of computational chemistry* **2004**, *25*, 1157-1174.
31. Lin, T.-Y.; Gross, W.S.; Auer, G.K.; Weibel, D.B. Cardiolipin alters Rhodobacter sphaeroides cell shape by affecting peptidoglycan precursor biosynthesis. *Mbio* **2019**, *10*.
32. Leneveu-Jenvrin, C.; Connil, N.; Bouffartigues, E.; Papadopoulos, V.; Feuilloley, M.G.; Chevalier, S. Structure-to-function relationships of bacterial translocator protein (TSPO): a focus on Pseudomonas. *Frontiers in microbiology* **2014**, *5*, 631.
33. Karshikoff, A.; Nilsson, L.; Ladenstein, R. Rigidity versus flexibility: the dilemma of understanding protein thermal stability. *The FEBS journal* **2015**, *282*, 3899-3917.

34. Šali, A.; Blundell, T.L. Comparative protein modelling by satisfaction of spatial restraints. *Journal of molecular biology* **1993**, *234*, 779-815.
35. Shen, M.y.; Sali, A. Statistical potential for assessment and prediction of protein structures. *Protein science* **2006**, *15*, 2507-2524.
36. John, B.; Sali, A. Comparative protein structure modeling by iterative alignment, model building and model assessment. *Nucleic acids research* **2003**, *31*, 3982-3992.
37. Harayama, T.; Riezman, H. Understanding the diversity of membrane lipid composition. *Nature Ecology & Evolution* **2018**, 1-18.
38. Hicks, A.M.; DeLong, C.J.; Thomas, M.J.; Samuel, M.; Cui, Z. Unique molecular signatures of glycerophospholipid species in different rat tissues analyzed by tandem mass spectrometry. *Biochimica et Biophysica Acta (BBA)-Molecular and Cell Biology of Lipids* **2006**, *1761*, 1022-1029.
39. Kiebish, M.A.; Han, X.; Seyfried, T.N. Examination of the brain mitochondrial lipidome using shotgun lipidomics. In *Lipidomics*, Springer: 2009; pp. 3-18.
40. Olofsson, G.; Sparr, E. Ionization constants pK a of cardiolipin. *PloS one* **2013**, *8*, e73040.
41. Van Der Spoel, D.; Lindahl, E.; Hess, B.; Groenhof, G.; Mark, A.E.; Berendsen, H.J. GROMACS: fast, flexible, and free. *Journal of computational chemistry* **2005**, *26*, 1701-1718.
42. Bussi, G.; Donadio, D.; Parrinello, M. Canonical sampling through velocity rescaling. *The Journal of chemical physics* **2007**, *126*, 014101.
43. Martoňák, R.; Laio, A.; Parrinello, M. Predicting Crystal Structures: The Parrinello-Rahman Method Revisited. *Physical Review Letters* **2003**, *90*, 075503, doi:10.1103/PhysRevLett.90.075503.
44. Van Aalten, D.M.; De Groot, B.L.; Findlay, J.B.; Berendsen, H.J.; Amadei, A. A comparison of techniques for calculating protein essential dynamics. *Journal of Computational Chemistry* **1997**, *18*, 169-181.
45. DeLano, W.L. Pymol: An open-source molecular graphics tool. *CCP4 Newsletter on protein crystallography* **2002**, *40*, 82-92.
46. Dahl, A.C.E.; Chavent, M.; Sansom, M.S. Bendix: intuitive helix geometry analysis and abstraction. *Bioinformatics* **2012**, *28*, 2193-2194.
47. Humphrey, W.; Dalke, A.; Schulten, K. VMD: visual molecular dynamics. *Journal of molecular graphics* **1996**, *14*, 33-38.
48. Lerner, M.; Carlson, H. APBS plugin for PyMOL. *Ann Arbor: University of Michigan* **2006**.
49. Song, W.; Duncan, A.; Corey, R.; Ansell, B. PyLipID. Availabe online: https://github.com/MareesAT/GWA_tutorial/ (accessed on